

www.acsami.org Research Article

Impact of Electrolyte Salts on Na Storage Performance for High-Surface-Area Carbon Anodes

Yiwei Li, Shiming Chen, Shenyang Xu, Zijian Wang, Kai Yang, Jiangtao Hu, Bo Cao, Wenguang Zhao, Mingjian Zhang, Luyi Yang,* and Feng Pan*



Cite This: ACS Appl. Mater. Interfaces 2021, 13, 48745–48752



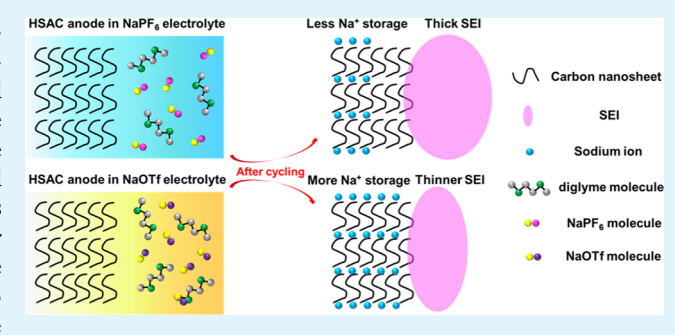
ACCESS

III Metrics & More

Article Recommendations

Supporting Information

ABSTRACT: High-surface-area carbon (HSAC) has been regarded as one of the most promising anode materials for sodiumion batteries. However, it generally suffers from low initial Coulombic efficiency (ICE), which is closely related to the formation process of a solid electrolyte interface (SEI). Herein, the impact of different electrolyte salts on the electrochemical performance and SEI formation of a commercial HSAC anode is studied. It is found that the use of NaCF₃SO₃ enables much higher ICE (69.28%) and reversible capacity (283 mA h g⁻¹) of the HSAC anode compared with the NaPF₆ electrolyte (59.65%, 243 mA h g⁻¹). Through comprehensive characterizations, the



improvement in electrochemical performance facilitated by NaCF₃SO₃ could be attributed to the reduced amount of Na_xC and the thinner SEI formed on the surface of HSAC during the initial cycle, which not only provides extra active sites for Na⁺ storage but also contributes to the promoted ICE. This work not only provides a deeper understanding of the role of electrolyte salt in SEI formation in the HSAC anode but also proposes a new method to further promote the ICE of the HSAC anode in sodium-ion batteries

KEYWORDS: electrolyte, solid electrolyte interface, high-surface-area carbon anode, sodium-ion batteries, initial Coulombic efficiency

■ INTRODUCTION

Energy storage has become one of the most important issues in recent years, and different kinds of energy storage systems have gradually sprung up.1 Lithium-ion batteries (LIBs), owing to their high energy density, environmental friendliness, and high safety, have been widely utilized in electronic devices and electric vehicles.^{2–4} Concerned by the increasing consumption rate of lithium resources, 5 researchers have considered sodiumion batteries (SIBs) as a promising candidate to substitute LIBs in the future due to their low cost.⁶⁻⁹ Carbon-based materials, including hard carbon and high-surface-area carbon (HSAC), have been widely reported owing to their low price, high stability, light weight, and high energy density. 10-14 Compared with hard carbon, the HSAC anode with a porous structure displayed better rate performance and cycling stability. 15-18 However, it still suffers from low initial Coulombic efficiency (ICE), which severely restricts its practical applications.

The value of ICE for carbon-based anodes is determined by the solid electrolyte interface (SEI) formation process, which could be manipulated by tuning the electrolyte components. In the previous reports, an electrolyte with ether solvent was beneficial to carbon anodes by promoting their electrochemical performance, including graphite and hard carbon. In recent years, it has been reported that the ICE and

reversible capacity of the HSAC anode can be greatly boosted by choosing ether-based solvents over ester-based ones. ^{26,27} It has also been reported that the better reversibility and cyclability of the hard carbon anode could be achieved in NaPF₆ electrolyte compared with NaClO₄ electrolyte (ester solvent). ²⁸ In addition, Passerini et al. found that the organic and inorganic components in the SEI of the hard carbon anode was affected by the Na salts in the electrolyte. ²⁹ However, few reports have focused on the impact of Na salts on the electrochemical performance and SEI for HSAC anodes until now.

Herein, we comprehensively analyzed the impact of Na salts on the electrochemical performance of a commercial HSAC anode in an ether electrolyte by comparing two different Na salts: sodium hexafluorophosphate (NaPF₆) salt and sodium trifluoromethanesulfonate (NaCF₃SO₃, which could be also written as NaOTf). The ICE and reversible capacity have been obviously promoted in the NaOTf electrolyte when compared

Received: July 28, 2021 Accepted: September 29, 2021 Published: October 8, 2021





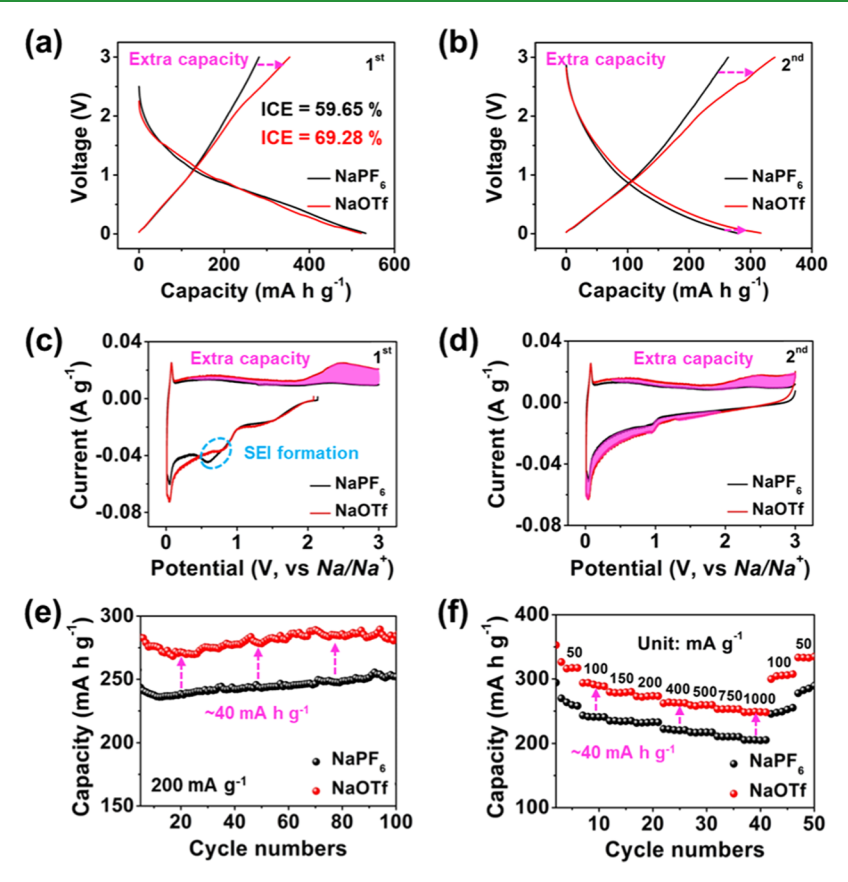


Figure 1. (a) First and (b) second capacity-voltage profiles of the HSAC anode in NaPF₆ and NaOTf electrolytes at 50 mA g⁻¹ (the extra capacity between NaPF₆ and NaOTf electrolytes is marked by pink dashed arrows). (c) First and (d) second cycles of CV curves for the HSAC anode in NaPF₆ and NaOTf electrolytes at 0.1 mV s⁻¹ (the peaks related to SEI are marked by blue dashed circle, and the extra capacity of the HSAC anode between NaPF₆ and NaOTf electrolytes is marked by pink shadow). (e) Cycling performance with a current density of 200 mA g⁻¹ (after 3 cycle activation at 50 mA g⁻¹) and (f) rate performance of the HSAC anode in NaPF₆ and NaOTf electrolytes (about 40 mA h g⁻¹ discrepancy of the HSAC anode between NaPF₆ and NaOTf electrolytes is marked by pink dashed arrows).

with the NaPF₆ electrolyte. Combined with electrochemical impedance, transmission electron microscopy (TEM), and Xray photoelectron spectroscopy (XPS) results, we discovered that in the NaPF₆ electrolyte, large amounts of Na_xC, an electrochemically inert compound, was formed on the HSAC anode during the initial cycle. By contrast, a thinner SEI, less Na_xC, and more reversible Na⁺ can be achieved in HSAC anodes when cycled in the NaOTf electrolyte, resulting in a large ICE and higher reversible capacity.

■ EXPERIMENTAL SECTION

Preparation of HSAC and Hard Carbon. The HSAC (XFP05, XFNANO, China) and hard carbon (Guangdong Canrd New Energy Technology Co., Ltd., China) were directly utilized without any further treatment.

Characterization Methods. X-ray diffraction with Cu K α (XRD, Bruker D8-Advance diffractometer, $\lambda = 1.5405 \text{ Å}$) was utilized to test the structure of HSAC. The morphology of the HSAC anode before and after cycling was determined by a scanning electron microscope (SEM, ZEISS Supra 55 field-emission scanning electron microscopy) and a transmission electron microscope (TEM, FEI TecnaiG2 F30). The corresponding element content was analyzed by an attached energy dispersive spectrometer (EDS). The detailed structure of the HSAC at the atomic scale was performed by a high-resolution transmission electron microscope (HRTEM). The specific surface areas of HSAC and hard carbon were tested by an adsorption and specific surface area tester (Micromeritics ASAP 2020M+C) by a nitrogen adsorption/desorption method, and the pore size distribution was analyzed by the adsorption isotherm according to the Barrett-Joyner-Halenda (BJH) model. X-ray photoelectron spectroscopy (XPS, ESCALAB 250XL) measurements were used to analyze the element distribution on the surface of the HSAC anode before and after cycling. The electrodes were washed with dimethyl carbonate (DMC) solvent to remove the contaminants on the surface and then dried in the glovebox for XPS measurements. All of the samples have been transferred in vacuum and etched by Ar⁺ ions for 60 s before testing. During XPS measurements, the base pressure of the sample chamber was kept below 3.0×10^{-10} mbar.

Electrochemical Testing. HSAC, acetylene black, and poly-(vinylidene fluoride) (PVDF) were poured into N-methyl pyrrolidone (NMP) solvent with a weight ratio of 7:2:1. The mixture was stirred for 10 h to obtain a uniform slurry. Then, the slurry was spread on Cu foil and dried at 120 °C in a vacuum oven. Coin cells (CR2032) were assembled in an argon-filled glovebox with water and oxygen below 1 ppm. Pure sodium and glass fiber (Whatman GF/A) were utilized as the counter electrode and separator, respectively. The electrode was cycled in the electrolyte of 1 M sodium hexafluorophosphate (NaPF₆) in diethylene glycol dimethyl ether and 1 M sodium trifluoromethanesulfonate (NaOTf) in diethylene glycol dimethyl ether, respectively. The as-prepared cells were equally discharged and charged between 0.01 and 3.0 V by a NEWARE system. Cyclic voltammetry (CV) and electrochemical impedance tests have been collected by an electrochemistry workstation (1400 cell test system, Solartron).

RESULTS AND DISCUSSION

The detailed information of as-prepared HSAC is shown in Figures S1 and S2. As shown in Figure S1a, a wide (002) peak could be observed at around 21.4°, corresponding to

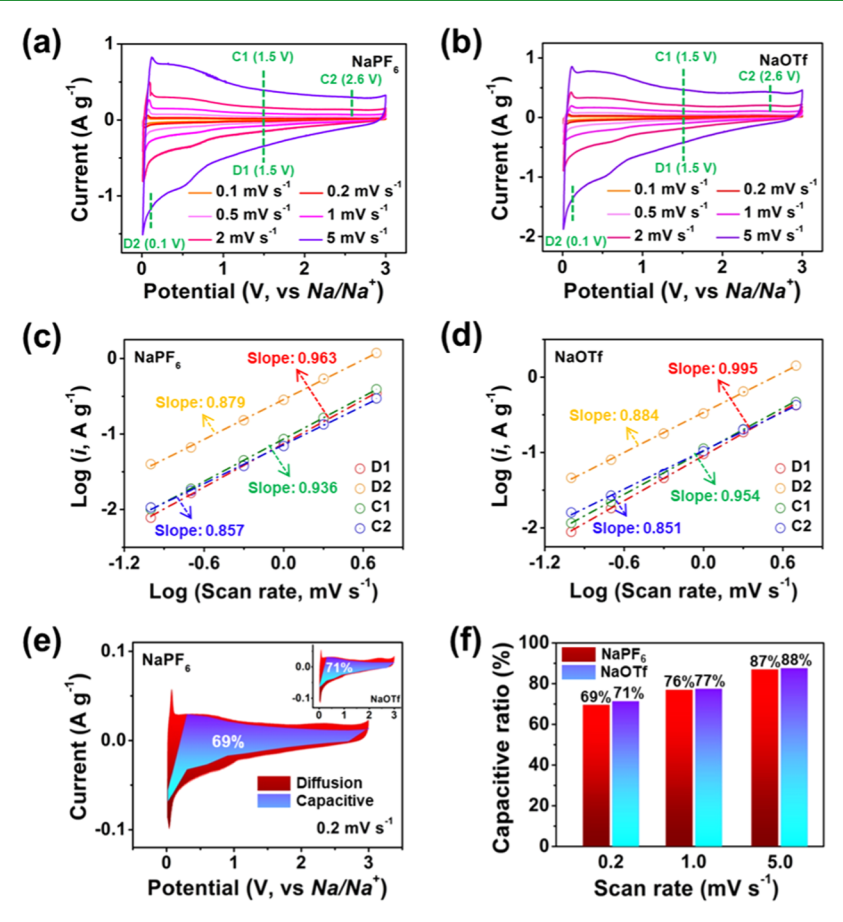


Figure 2. (a)–(b) Normalized CV curves at different scan rates $(0.1, 0.2, 0.5, 1, 2, \text{ and } 5 \text{ mV s}^{-1})$ of the HSAC anode in (a) NaPF₆ and (b) NaOTf electrolytes. (c)–(d) Fitted linear relationship between $\log(i)$ and $\log(\nu)$ and the calculated b values at the selected voltage conditions (marked by green dashed lines in (a) and (b)) in (c) NaPF₆ and (d) NaOTf electrolytes. (e) Capacitive contribution in the CV curves of the HSAC anode in NaPF₆ and NaOTf (inset on the top right corner) at a scan rate of 0.2 mV s⁻¹. (f) Capacitive contribution ratio of the HSAC anode in NaPF₆ and NaOTf at different scan rates $(0.2, 1, \text{ and } 5 \text{ mV s}^{-1})$.

disordered carbon layers in HSAC with an average layer distance of ~4.16 Å. The XPS spectra of C 1s (Figure S1b) can be divided into four peaks that correspond to C-C, C-H, C-O, and C=O, respectively.²⁹ The SEM image of HSAC (Figure S1c) exhibits a porous structure, consisting of mesopores and macropores, as shown in the TEM image (Figure S1d), which is beneficial to Na⁺ diffusion. The HRTEM image and the corresponding fast Fourier transform (FFT) of HSAC (Figure S1e) exhibit an average distance between carbon layers of 4.292 Å as well as no distinct diffraction patterns, which is in good agreement with the XRD result in Figure S1a. The specific surface area and the distribution of pore size of HSAC are also measured (Figure S2). On the one hand, HSAC exhibits a specific surface area of 293.85 m 2 g $^{-1}$, which enables Na $^+$ storage on the surface (Figure S2a); 30 on the other hand, HSAC mainly contains macropores (100 nm) and a small amount of meso/ micropores, which is beneficial to the fast diffusion of Na+ (Figure S2b).31

The electrochemical performance of the HSAC anode in NaPF₆ and NaOTf electrolytes is shown in Figure 1. During the initial cycle (Figure 1a), NaPF₆ and NaOTf electrolytes delivered similar initial discharge capacities (about 565 mA h g⁻¹). In addition, the capacity–voltage profile of the HSAC anode is slopping in the whole voltage range, implying that the Na⁺ storage process is capacitive-dominated. Nevertheless, the initial charging capacity in the NaOTf electrolyte is higher than

that in the NaPF₆ electrolyte, corresponding to an improved ICE (from 59.65 to 69.28%). The promoted ICE for the HSAC anode in the NaOTf electrolyte is higher than most of the previously reported HSAC anodes, as shown in Table S1. More importantly, the extra capacity in the NaOTf electrolyte is retained at the second cycle (Figure 1b). A similar phenomenon could be discovered in the normalized CV results, (Figure 1c,d), where the absence of sharp redox peaks implies the capacitive-controlled behavior and the extra charge (colored area) obtained in the NaOTf electrolyte is in line with the extra capacity. It should be noted that a broad reduction peak at around 0.7 V can be observed (Figure 1c), which is attributed to the irreversible SEI formation. The intensity of this peak for the NaOTf electrolyte is lower than that for the NaPF₆ electrolyte, suggesting less electrolyte is consumed to form SEI in the NaOTf electrolyte, which is beneficial to a higher ICE. Figure 1e shows the cycling performance of the HSAC anode in NaPF₆ and NaOTf electrolytes at a higher specific current (200 mA g⁻¹, after 3 cycles activation at 50 mA 1). The HSAC anode in the NaOTf electrolyte exhibits a higher initial capacity (283 mA h g⁻¹) than that in the NaPF₆ electrolyte. During long-term cycling, capacity decay could be barely observed in both cells after 100 cycles (capacity-voltage profiles are shown in Figure S3), demonstrating the superior cycling performance of the HSAC anode as well as the high reversibility of the extra capacity (~40 mA h g⁻¹). Meanwhile, the rate performance of the HSAC anode cycled in different

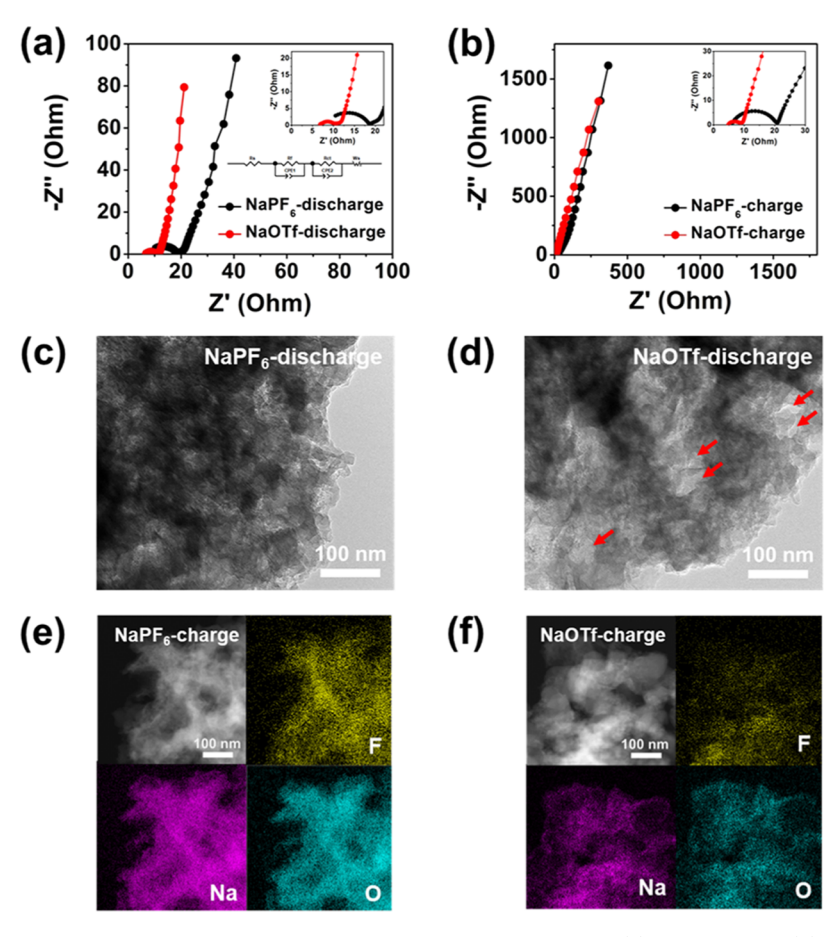


Figure 3. (a)-(b) Electrochemical impedance spectra of the HSAC electrode after the initial (a) discharge and (b) charge process in NaPF₆ and NaOTf electrolytes (from 0.01 to 100 000 Hz). The corresponding enlarged semicircles are shown in the insets. The circuit model for fitting the impedance semicircles is shown in the inset of (a). (c)-(d) TEM images of the HSAC anode after the initial discharge process in (c) NaPF₆ and (d) NaOTf electrolytes. The nanopores in (d) are marked by red arrows. (e)-(f) TEM image and the corresponding element distribution of Na, F, and O in the HSAC anode after the initial charge in (e) NaPF₆ and (f) NaOTf electrolytes.

electrolytes (Figures 1f and S4) shows that the extra capacity is not affected by charge/discharge rates, inferring fast reaction kinetics.

As mentioned above, higher ICE and reversible capacity have been achieved for the HSAC anode with the help of NaOTf. To further explore whether the promoted electrochemical performance in the NaOTf electrolyte is characteristic for HSAC, commercial hard carbon has been chosen as the comparison group. Interestingly, no distinct difference could be observed in NaPF₆ and NaOTf electrolytes (Figure S5). Considering that hard carbon possesses a much lower specific surface area (2.79 m² g⁻¹) than HSAC (see detailed data in Figure S6), the promoted electrochemical performance observed in the HSAC anode might be attributed to the unique Na+ storage behavior originated from its porous structure and high specific surface area.

To further understand the Na+ storage behavior of the HSAC anode in NaPF6 and NaOTf electrolytes, the normalized CV curves with different scan rates are shown in Figure 2a,b, respectively. The charge storage of diffusioncontrolled and capacitive-controlled processes could be analyzed by

$$i(V) = a\nu^b \tag{1}$$

where i(V) represents the corresponding current at the specific voltage and ν represents the corresponding scan rate.³²

the a and b values could be obtained by the intercept and slope of the $\log(i)$ versus $\log(\nu)$ plot. When the b value is close to 0.5, the process is close to diffusion-controlled and when the bvalue is close to 1, the process is close to capacitivecontrolled.³⁰ Four different conditions (D1, D2, C1, and C2) have been selected to compare the Na⁺ storage behavior in NaPF₆ and NaOTf electrolytes, and the corresponding fitting curves with the calculated slope are shown in Figure 2c,d. The b values for different conditions range between 0.851 and 0.995, suggesting the Na⁺ storage behaviors for HSAC in different electrolytes are mainly capacitive-controlled. Additionally, according to the equation

$$i(V) = k_1 \nu + k_2 \nu^{1/2} \tag{2}$$

the diffusion-controlled and capacitive-controlled capacity could also be quantitatively calculated.³³ $k_1\nu$ and $k_2\nu^{1/2}$ correspond to the capacitive-controlled and diffusion-controlled contributions to the total current, respectively. The specific contribution at the specific potential could be quantified through confirming $\bar{k_1}$ and $\bar{k_2}$. Figure 2e shows that under a scan rate of 0.2 mV s⁻¹, the capacitive contributions in NaOTf and NaPF6 are 71 and 69%, respectively. In addition, the capacitive contributions will gradually increase with the scan rate (Figure 2f), which agrees with the previous results.³⁴ From the results above, it could be concluded that the Na⁺ storage behavior for the HSAC anode

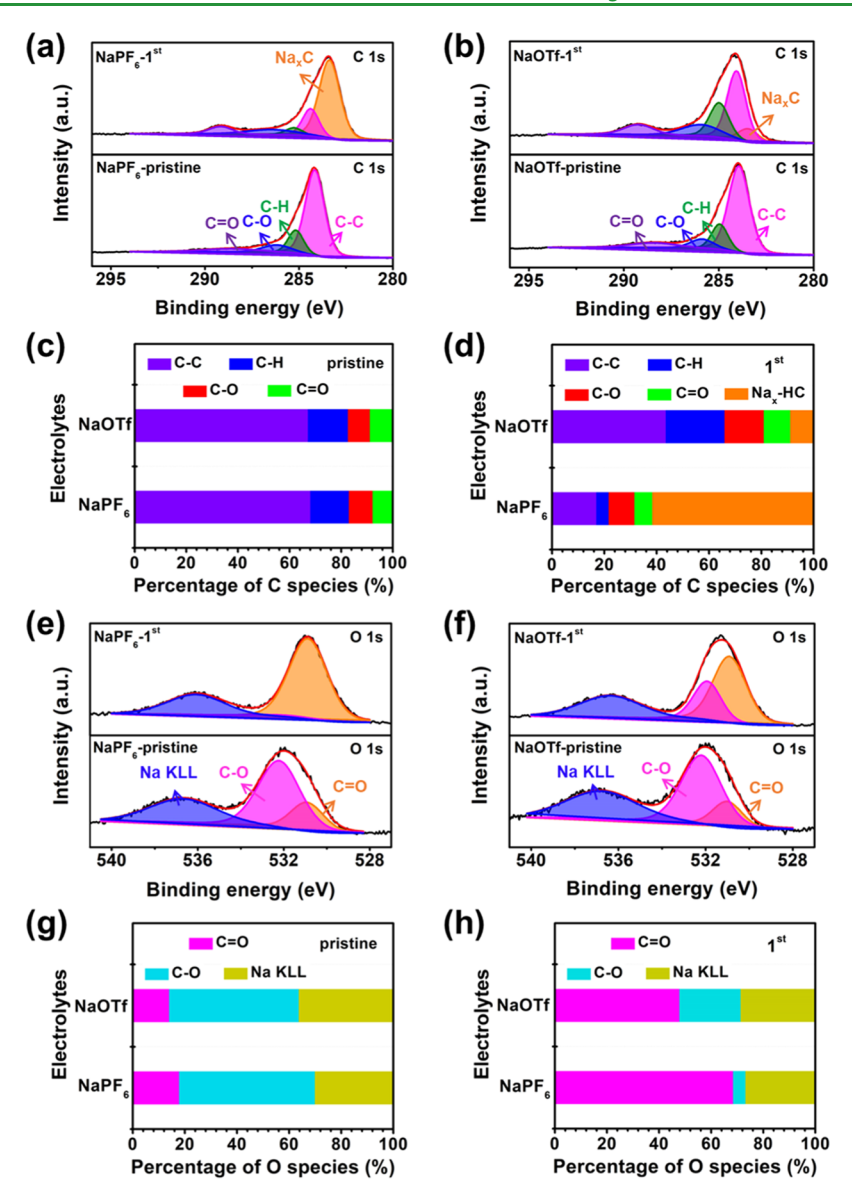


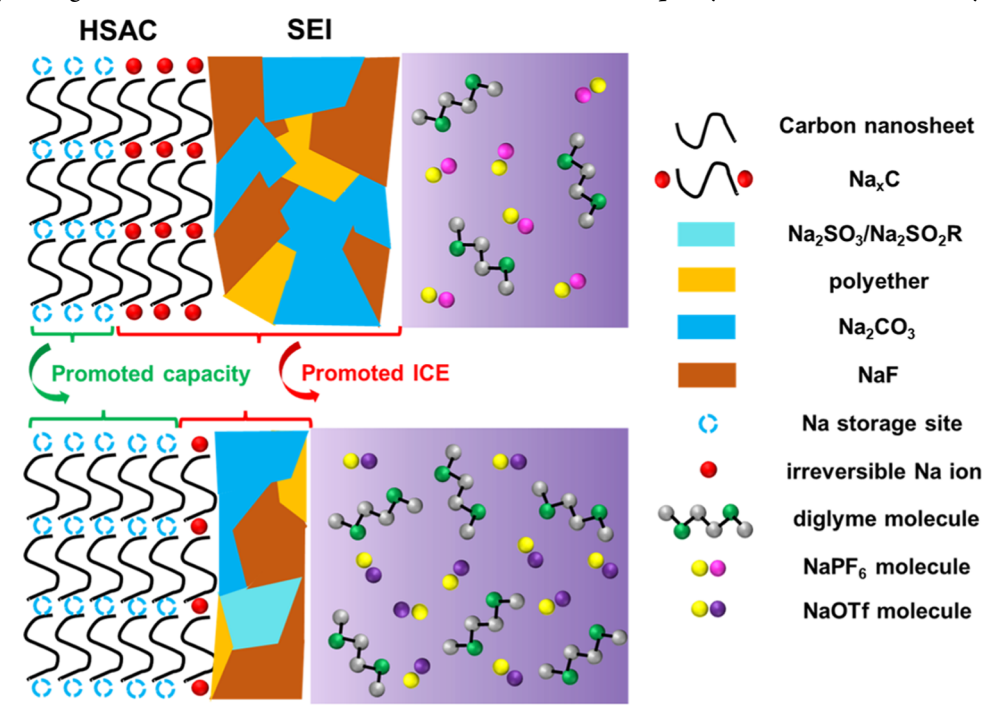
Figure 4. (a)—(b) XPS spectra of the C 1s signal for the HSAC electrode immersed (pristine) and after the initial cycle (charged to 3 V) in (a) NaPF₆ and (b) NaOTf electrolytes. The Na_xC, C-C, C-H, C-O, and C=O peaks are marked by orange, pink, green, blue, and purple arrows, respectively. (c)—(d) Specific ratios of Na_xC, C-C, C-H, C-O, and C=O bonds calculated by the fitted peak area in (a) and (b): (c) immersed in NaPF₆ and NaOTf electrolytes and (d) after the initial cycle. (e)—(f) XPS spectra of the O 1s signal for the HSAC electrode immersed (pristine) and after the initial cycle in (e) NaPF₆ and (f) NaOTf electrolytes. The C=O, C-O, and Na KLL peaks are marked by orange, pink, and blue arrows, respectively. (g)—(h) Specific ratios of C=O, C-O, and Na KLL bonds calculated by the fitted peak area in (e) and (f): (g) immersed in NaPF₆ and NaOTf electrolytes and (h) after the initial cycle.

is mainly capacitive-controlled, regardless of the choice of Na salts. To further prove that the Na⁺-ion storage behavior is capacitive-controlled, HRTEM images of the HSAC electrode before and after the initial discharge and charge are shown in Figure S7. The layer distance of the HSAC anode barely changed after the initial discharge and charge in both NaPF₆ and NaOTf electrolytes, further demonstrating that the electrochemical behavior for the HSAC anode is capacitive-controlled. Therefore, the electrochemical behavior of HSAC is dominated by the surface adsorption and pore-filling processes, which are closely associated with the formation of SEI

The SEI of the HSAC anode in NaPF₆ and NaOTf electrolytes is then analyzed by electrochemical impedance spectroscopy and *ex situ* TEM. The impedance spectra of

HSAC anodes after the initial discharge/charge process are shown in Figure 3a,b. According to our fitting results (the corresponding equivalent circuit is shown in the inset of Figure 3a), both interfacial resistance ($R_{\rm f}$) and charge-transfer resistance ($R_{\rm ct}$) for the HSAC anode in the NaPF₆ electrolyte are larger than those in NaOTf after the initial discharge and charge process (Table S2), implying that a thicker SEI formed in the NaPF₆ electrolyte. This could be confirmed by the TEM images (Figure 3c,d) of HSAC electrodes after the initial discharge process (the TEM images of the HSAC electrode before cycling are shown in Figure S8). The distinct porous structure disappeared after the initial discharge in the NaPF₆ electrolyte owing to the formation of SEI. However, part of the nanopores could still be retained after the initial discharge in the NaOTf electrolyte, implying less SEI has formed. TEM

Scheme 1. Illustration of the Different SEI Formed on the Surface of the HSAC Electrode in NaPF₆ and NaOTf Electrolytes and the Corresponding Mechanism of the Promoted ICE and Reversible Capacity in the NaOTf Electrolyte



images with the corresponding EDS mapping images of Na, F, and O elements in the HSAC anode after the initial charge in NaPF₆ and NaOTf electrolytes are also shown in Figure 3e,3f (the corresponding EDS mapping images of P and S are shown in Figure S9), and the specific element ratio is shown in Table S3. The contents of Na, F, and O detected on HSAC cycled in NaOTf are less than those in the NaPF₆ electrolyte, inferring a thinner SEI. Similar results can be observed in SEM images and the corresponding element distribution of HSAC anodes (Figure S10 and Table S4). Therefore, the improved ICE for the HSAC anode in NaOTf electrolyte could be ascribed to the thinner SEI formed on the surface.

To further analyze the chemical composition of SEI on the HSAC electrode, ex situ XPS measurements have been performed. The XPS spectra of the HSAC electrode after the initial discharge and charge are shown in Figure S11, where the ratios of C:O, C:Na, and C:F for the HSAC electrode in the NaPF₆ electrolyte are higher than those in the NaOTf electrolyte, further demonstrating the thinner SEI formed in the NaOTf electrolyte. The XPS spectra of the C 1s signal for HSAC electrodes before cycling (immersed in NaPF₆ and NaOTf electrolytes, respectively) and after the initial cycle in different electrolytes are shown in Figure 4a,b; each signal has been etched for 60 s by Ar⁺ to remove the contaminants on the surface. Each peak can be divided into five peaks located at 283.5, 284.6, 285.2, 286.2, and 288 eV, corresponding to the Na_xC, C-C, C-H, C-O, and C=O bonds, respectively. The intensity of the C-C peak decreased, and other peaks (e.g., C-O and C=O) related to SEI components increased after the initial cycle, implying the formation of SEI after the initial cycle. Compared with the NaPF₆ electrolyte, the stronger intensity of the C-C bond for the HSAC electrode cycled in the NaOTf electrolyte could be observed, implying that less SEI component formed on the surface, which means thinner SEI on the surface of the HSAC anode in the NaOTf electrolyte. To further explore the variation on the

surface of the HSAC electrode after the initial charge, the corresponding C 1s spectra in NaPF₆ and NaOTf electrolytes without etching are shown in Figure S12. Interestingly, a small amount of sodiated HSAC (Na_xC) could be discovered after the initial cycle in the NaOTf electrolyte, which could not be observed in the NaPF₆ electrolyte. Considering that Na_xC is formed underneath SEI,²⁸ it is inferred that a thinner SEI is formed on the surface of the HSAC anode in the NaOTf electrolyte, which is consistent with the previous results.

For quantitative analysis, the ratios of Na_xC, C-C, C-H, C-O, and C=O bonds after etching are calculated by their corresponding peak areas (Figure 4c,d). The ratios of C-C, C-H, C-O, and C=O are similar for the HSAC electrodes immersed in NaPF6 and NaOTf electrolytes (Figure 4c). However, after the initial cycle, a larger amount of Na, C could be measured on the surface of the HSAC electrode cycled in the NaPF₆ electrolyte, which is much severe than in the NaOTf electrolyte (Figure 4d). Considering that Na ions in Na_rC are electrochemically inert (the Na ions could still be observed after full charging, meaning that the Na ions in Na_xC are inert), ²⁹ part of the inserted Na⁺ during discharging could not be extracted from the HSAC electrode, leading to a low ICE. In addition, the large number of Na_xC on the surface of the HSAC anode in the NaPF₆ electrolyte will contribute to a large amount of invalid Na+ storage sites, which causes the low reversible capacity in the following cycles. Therefore, the HSAC anode in the NaPF₆ electrolyte exhibits less ICE and reversible capacity compared to those in the NaOTf electrolyte. Moreover, from the O 1s spectra for HSAC electrodes (Figure 4e-4h), it could be observed that the C-O:C=Oratio decreased after the initial cycle in both electrolytes. Since C-O could be originated from the residue electrolyte or polyether SEI component while C=O is attributed to the formation of Na₂CO₃/Na₂CO₂R/Na₂SO₂R compounds, the different specific contents of C-O and C=O for the HSAC electrode cycled in NaPF₆ and NaOTf electrolytes suggest that

the composition of organic SEI varies in the two electrolytes (Figure 4g,h). It should be noted that as another common SEI constituent, NaF in both SEI layers is similar (Figure S13).

Based on the above results and discussions, different SEI formation behaviors of the HSAC anode cycled in NaPFs and NaOTf electrolytes are schematically illustrated in Scheme 1. A thick SEI containing NaF, C=O compounds (Na₂CO₃/ Na₂CO₂R), and polyether formed on the surface of the HSAC electrode in the NaPF6 electrolyte. Besides, a large amount of electrochemically inert compound Na_rC formed on the surface, which causes the consumption of sodium ions, together with the formation of SEI, contributing to a low ICE in the NaPF₆ electrolyte. By contrast, fewer C=O compounds (Na2CO2/Na2CO2R/Na2SO2R) and Na2C are formed on the surface of the HSAC anode in the NaOTf electrolyte, which contributes to a thinner SEI and more active sites for Na+ storage, effectively promoting the ICE and reversible capacity of the HSAC electrode during long-term cycles.

CONCLUSIONS

The different electrochemical performances of the commercial HSAC electrode in NaPF₆ and NaOTf electrolytes have been systematically researched. It is found that the use of NaCF₃SO₃ enables much higher ICE and reversible capacity of HSAC compared with the NaPF₆ electrolyte. The promoted electrochemical performance in the NaOTf electrolyte can be explained by the different surface behaviors: a thinner SEI and smaller amount of Na_xC formed on the surface of HSAC in NaOTf, which jointly contributes to less Na consumption during the initial cycle as well as facilitates more electrochemically active sites, causing higher ICE and more reversible capacity during long-term cycling. By revealing the correlation between the electrolyte and the electrochemical performance, this work provides useful insights into the optimization of the electrolyte/electrode interface and the promotion of electrochemical performance in carbon-based anodes for SIBs.

ASSOCIATED CONTENT

Supporting Information

The Supporting Information is available free of charge at https://pubs.acs.org/doi/10.1021/acsami.1c14334.

XRD patterns, SEM images, TEM images, XPS spectra, N_2 adsorption/desorption isotherm and pore size distribution results, specific capacity—voltage profiles with different cycles and different rates of the HSAC anode, and initial capacity—voltage profile of hard carbon anode (PDF)

AUTHOR INFORMATION

Corresponding Authors

Luyi Yang — School of Advanced Materials, Shenzhen Graduate School, Peking University, Shenzhen 518055, People's Republic of China; orcid.org/0000-0002-5516-9829; Email: yangly@pkusz.edu.cn

Feng Pan — School of Advanced Materials, Shenzhen Graduate School, Peking University, Shenzhen 518055, People's Republic of China; ⊚ orcid.org/0000-0002-8216-1339; Email: panfeng@pkusz.edu.cn

Authors

- Yiwei Li School of Advanced Materials, Shenzhen Graduate School, Peking University, Shenzhen 518055, People's Republic of China
- Shiming Chen School of Advanced Materials, Shenzhen Graduate School, Peking University, Shenzhen 518055, People's Republic of China
- Shenyang Xu School of Advanced Materials, Shenzhen Graduate School, Peking University, Shenzhen 518055, People's Republic of China
- Zijian Wang School of Advanced Materials, Shenzhen Graduate School, Peking University, Shenzhen 518055, People's Republic of China
- Kai Yang School of Advanced Materials, Shenzhen Graduate School, Peking University, Shenzhen 518055, People's Republic of China
- Jiangtao Hu School of Advanced Materials, Shenzhen Graduate School, Peking University, Shenzhen 518055, People's Republic of China
- Bo Cao School of Advanced Materials, Shenzhen Graduate School, Peking University, Shenzhen 518055, People's Republic of China
- Wenguang Zhao School of Advanced Materials, Shenzhen Graduate School, Peking University, Shenzhen 518055, People's Republic of China
- Mingjian Zhang School of Advanced Materials, Shenzhen Graduate School, Peking University, Shenzhen 518055, People's Republic of China; orcid.org/0000-0002-6843-5911

Complete contact information is available at: https://pubs.acs.org/10.1021/acsami.1c14334

Notes

The authors declare no competing financial interest.

ACKNOWLEDGMENTS

The authors acknowledge support from the National Key R&D Program of China (2016YFB0700600), the Shenzhen Science and Technology Research Grant (No. JCYJ20200109140416788), the Chemistry and Chemical Engineering Guangdong Laboratory (Grant No. 1922018), and the National Key R&D Program of China (2020YFB0704500).

REFERENCES

- (1) Sui, D.; Chang, M. J.; Wang, H. Y.; Qian, H.; Yang, Y. L.; Li, S.; Zhang, Y. S.; Song, Y. Z. A Brief Review of Catalytic Cathode Materials for Na-CO₂ Batteries. *Catalysts* **2021**, *11*, 603.
- (2) Zhuo, Z.; Dai, K.; Qiao, R.; Wang, R.; Wu, J.; Liu, Y.; Peng, J.; Chen, L.; Chuang, Y.-d.; Pan, F.; Shen, Z.-x.; Liu, G.; Li, H.; Devereaux, T. P.; Yang, W. Cycling Mechanism of Li₂MnO₃: Li-CO₂ Batteries and Commonality on Oxygen Redox in Cathode Materials. *Joule* **2021**, *5*, 975–997.
- (3) Manthiram, A. A Reflection on Lithium-Ion Battery Cathode Chemistry. *Nat. Commun.* **2020**, *11*, No. 1550.
- (4) Liu, K.; Liu, Y.; Lin, D.; Pei, A.; Cui, Y. Materials for Lithium-Ion Battery Safety. Sci. Adv. 2018, 4, No. eaas9820.
- (5) Han, M. H.; Gonzalo, E.; Singh, G.; Rojo, T. A Comprehensive Review of Sodium Layered Oxides: Powerful Cathodes for Na-Ion Batteries. *Energy Environ. Sci.* **2015**, *8*, 81–102.
- (6) Kundu, D.; Talaie, E.; Duffort, V.; Nazar, L. F. The Emerging Chemistry of Sodium Ion Batteries for Electrochemical Energy Storage. *Angew. Chem., Int. Ed.* **2015**, *54*, 3431–3448.

- (7) Vaalma, C.; Buchholz, D.; Weil, M.; Passerini, S. A Cost and Resource Analysis of Sodium-Ion Batteries. *Nat. Rev. Mater.* **2018**, *3*, No. 18013.
- (8) Yabuuchi, N.; Kubota, K.; Dahbi, M.; Komaba, S. Research Development on Sodium-Ion Batteries. *Chem. Rev.* **2014**, *114*, 11636–11682.
- (9) Niu, Y. B.; Guo, Y. J.; Yin, Y. X.; Zhang, S. Y.; Wang, T.; Wang, P.; Xin, S.; Guo, Y. G. High-Efficiency Cathode Sodium Compensation for Sodium-Ion Batteries. *Adv. Mater.* **2020**, 32, No. 2001419.
- (10) Shan, C.; Feng, X.; Yang, J.; Yang, X.; Guan, H.-Y.; Argueta, M.; Wu, X.-L.; Liu, D.-S.; Austin, D. J.; Nie, P.; Yue, Y. Hierarchical Porous Carbon Pellicles: Electrospinning Synthesis and Applications as Anodes for Sodium-Ion Batteries with an Outstanding Performance. *Carbon* **2020**, *157*, 308–315.
- (11) Zhang, Y.; Chen, L.; Meng, Y.; Xie, J.; Guo, Y.; Xiao, D. Lithium and Sodium Storage in Highly Ordered Mesoporous Nitrogen-Doped Carbons Derived from Honey. *J. Power Sources* **2016**, 335, 20–30.
- (12) Shen, F.; Luo, W.; Dai, J.; Yao, Y.; Zhu, M.; Hitz, E.; Tang, Y.; Chen, Y.; Sprenkle, V. L.; Li, X.; Hu, L. Ultra-Thick, Low-Tortuosity, and Mesoporous Wood Carbon Anode for High-Performance Sodium-Ion Batteries. *Adv. Energy Mater.* **2016**, *6*, No. 1600377.
- (13) Xie, F.; Xu, Z.; Jensen, A. C. S.; Au, H.; Lu, Y.; Araullo-Peters, V.; Drew, A. J.; Hu, Y.-S.; Titirici, M.-M. Hard-Soft Carbon Composite Anodes with Synergistic Sodium Storage Performance. *Adv. Funct. Mater.* **2019**, 29, No. 1901072.
- (14) Li, Y.; Hu, J.; Wang, Z.; Yang, K.; Huang, W.; Cao, B.; Li, Z.; Zhang, W.; Pan, F. Low-Temperature Catalytic Graphitization to Enhance Na-Ion Transportation in Carbon Electrodes. ACS Appl. Mater. Interfaces 2019, 11, 24164–24171.
- (15) Liu, P.; Li, Y.; Hu, Y.-S.; Li, H.; Chen, L.; Huang, X. A Waste Biomass Derived Hard Carbon as a High-Performance Anode Material for Sodium-Ion Batteries. *J. Mater. Chem. A* **2016**, *4*, 13046–13052.
- (16) Thompson, B. R.; Horozov, T. S.; Stoyanov, S. D.; Paunov, V. N. Hierarchically Structured Composites and Porous Materials from Soft Templates: Fabrication and Applications. *J. Mater. Chem. A* **2019**, 7, 8030–8049.
- (17) Shao, W.; Hu, F.; Liu, S.; Zhang, T.; Song, C.; Weng, Z.; Wang, J.; Jian, X. Carbon Spheres with Rational Designed Surface and Secondary Particle-Piled Structures for Fast and Stable Sodium Storage. J. Energy Chem. 2021, 54, 368–376.
- (18) Liu, Y.; Fan, F.; Wang, J.; Liu, Y.; Chen, H.; Jungjohann, K. L.; Xu, Y.; Zhu, Y.; Bigio, D.; Zhu, T.; Wang, C. In Situ Transmission Electron Microscopy Study of Electrochemical Sodiation and Potassiation of Carbon Nanofibers. *Nano Lett.* **2014**, *14*, 3445–3452.
- (19) Li, Q.; Zhu, Y.; Zhao, P.; Yuan, C.; Chen, M.; Wang, C. Commercial Activated Carbon as a Novel Precursor of the Amorphous Carbon for High-Performance Sodium-Ion Batteries Anode. *Carbon* **2018**, *129*, 85–94.
- (20) Li, Y.; Xu, S.; Wu, X.; Yu, J.; Wang, Y.; Hu, Y.-S.; Li, H.; Chen, L.; Huang, X. Amorphous Monodispersed Hard Carbon Micro-Spherules Derived from Biomass as a High Performance Negative Electrode Material for Sodium-Ion Batteries. *J. Mater. Chem. A* **2015**, 3, 71–77.
- (21) He, Y.; Bai, P.; Gao, S.; Xu, Y. Marriage of an Ether-Based Electrolyte with Hard Carbon Anodes Creates Superior Sodium-Ion Batteries with High Mass Loading. *Acs Appl. Mater. Interfaces* **2018**, *10*, 41380–41388.
- (22) Bai, P.; He, Y.; Xiong, P.; Zhao, X.; Xu, K.; Xu, Y. Long Cycle Life and High Rate Sodium-Ion Chemistry for Hard Carbon Anodes. *Energy Storage Mater.* **2018**, *13*, 274–282.
- (23) Wang, E. H.; Niu, Y. B.; Yin, Y. X.; Guo, Y. G. Manipulating Electrode/Electrolyte Interphases of Sodium-Ion Batteries: Strategies and Perspectives. *ACS Mater. Lett.* **2021**, *3*, 18–41.
- (24) Goktas, M.; Bolli, C.; Berg, E. J.; Novak, P.; Pollok, K.; Langenhorst, F.; Roeder, M. V.; Lenchuk, O.; Mollenhauer, D.; Adelhelm, P. Graphite as Cointercalation Electrode for Sodium-Ion

- Batteries: Electrode Dynamics and the Missing Solid Electrolyte Interphase (SEI). Adv. Energy Mater. 2018, 8, No. 1702724.
- (25) Zhu, Y.-E.; Yang, L.; Zhou, X.; Li, F.; Wei, J.; Zhou, Z. Boosting the Rate Capability of Hard Carbon with an Ether-Based Electrolyte for Sodium Ion Batteries. *J. Mater. Chem. A* **2017**, *5*, 9528–9532.
- (26) Zhang, J.; Wang, D.-W.; Lv, W.; Zhang, S.; Liang, Q.; Zheng, D.; Kang, F.; Yang, Q.-H. Achieving Superb Sodium Storage Performance on Carbon Anodes through an Ether-Derived Solid Electrolyte Interphase. *Energy Environ. Sci.* **2017**, *10*, 370–376.
- (27) Zhen, Y.; Sa, R.; Zhou, K.; Ding, L.; Chen, Y.; Mathur, S.; Hong, Z. Breaking the Limitation of Sodium-Ion Storage for Nanostructured Carbon Anode by Engineering Desolvation Barrier with Neat Electrolytes. *Nano Energy* **2020**, *74*, No. 104895.
- (28) Dahbi, M.; Nakano, T.; Yabuuchi, N.; Fujimura, S.; Chihara, K.; Kubota, K.; Son, J. Y.; Cui, Y. T.; Oji, H.; Komaba, S. Effect of Hexafluorophosphate and Fluoroethylene Carbonate on Electrochemical Performance and the Surface Layer of Hard Carbon for Sodium-Ion Batteries. *ChemElectroChem* **2016**, *3*, 1856–1867.
- (29) Eshetu, G. G.; Diemant, T.; Hekmatfar, M.; Grugeon, S.; Behm, R. J.; Laruelle, S.; Armand, M.; Passerini, S. Impact of the Electrolyte Salt Anion on the Solid Electrolyte Interphase Formation in Sodium Ion Batteries. *Nano Energy.* **2019**, *55*, 327–340.
- (30) Li, S.; Qiu, J.; Lai, C.; Ling, M.; Zhao, H.; Zhang, S. Surface Capacitive Contributions: Towards High Rate Anode Materials for Sodium Ion Batteries. *Nano Energy* **2015**, *12*, 224–230.
- (31) Zhang, J.; Wang, D.-W.; Lv, W.; Qin, L.; Niu, S.; Zhang, S.; Cao, T.; Kang, F.; Yang, Q.-H. Ethers Illume Sodium-Based Battery Chemistry: Uniqueness, Surprise, and Challenges. *Adv. Energy Mater.* **2018**, *8*, No. 1801361.
- (32) Wang, L.; Bi, X.; Yang, S. Partially Single-Crystalline Mesoporous Nb₂O₅ Nanosheets in between Graphene for Ultrafast Sodium Storage. *Adv. Mater.* **2016**, *28*, 7672–7679.
- (33) Chen, Z.; Augustyn, V.; Jia, X.; Xiao, Q.; Dunn, B.; Lu, Y. High-Performance Sodium-Ion Pseudocapacitors Based on Hierarchically Porous Nanowire Composites. *ACS Nano* **2012**, *6*, 4319–4327.
- (34) Lu, P.; Sun, Y.; Xiang, H.; Liang, X.; Yu, Y. 3D Amorphous Carbon with Controlled Porous and Disordered Structures as a High-Rate Anode Material for Sodium-Ion Batteries. *Adv. Energy Mater.* **2018**, *8*, No. 1702434.
- (35) Kim, H.; Park, J. S.; Sahgong, S. H.; Park, S.; Kim, J. K.; Kim, Y. Metal-Free Hybrid Seawater Fuel Cell with an Ether-Based Electrolyte. *J. Mater. Chem. A* **2014**, *2*, 19584–19588.
- (36) Kanamura, K.; Shiraishi, S.; Takezawa, H.; Takehara, Z. XPS Analysis of the Surface of a Carbon Electrode Intercalated by Lithium Ions. *Chem. Mater.* **1997**, *9*, 1797–1804.
- (37) Philippe, B.; Hahlin, M.; Edstrom, K.; Gustafsson, T.; Siegbahn, H.; Rensmo, H. Photoelectron Spectroscopy for Lithium Battery Interface Studies. *J. Electrochem. Soc.* **2016**, *163*, A178–A191.